Section 2
Mechanisms and Modeling

5

Simulations of Optical Processes in Organic Photovoltaic Devices

Nils-Krister Persson and Olle Inganäs

Biomolecular and Organic Electronics, Department of Physics and Measurement Technology, Linköping University, Linköping, Sweden

Contents

Abstract By simulation of the optical processes in photovoltaic devices it is possible to enhance both the understanding of the physical processes occurring as a result of optical absorption and also to optimize the design of devices given this understanding. Calculations allow properties that are out of reach for direct measurements, such as absorption profiles, to be evaluated. Besides, in a relatively short time on a computer, thousands of different device geometries can be simulated. This is far beyond what can be performed experimentally, both from a time and a material householding perspective, and allows optimization of device design from an optical point of view. We present a modeling approach based on a number of assumptions such as homogeneous layers, sharp and planar interfaces, scattering free optics, coherence in the stack part of the device, and incoherence when adding energies across the substrate. The model has only layer thickness, layer dielectrical functions, and exciton diffusion length as input. Many different kinds of output are possible: absorption profile, reflectance, absorbance, absorption distribution, limits for quantum efficiencies, etc. The model is applied to devices with the active material being a pure polyfluorene–copolymer or blended with C_{60} as the acceptor.

Keywords optical modeling, polymer, organic, photovoltaic device, complex index of refraction, spectroscopic ellipsometry, polyfluorene, fullerene, blend

5.1. INTRODUCTION

The optical processes inside an organic photovoltaic device include electromagnetic wave transmission and reflection at all the interfaces found inside the device, and the decay of wave energy due to absorption inside the active photovoltaic layers, as well as other layers such as structural layers and electrodes. We can describe the processes in terms of incoupling and absorption of the incoming photon. As the layers found inside a polymer-based photovoltaic device (PPVD) are all thin, and the total thickness of the film part of a device may be of the order of one or two wavelengths of incoming light, wave phenomena are ubiquitous and must be properly accounted for when modeling the optical processes inside the PPVD. This can be done with a full dielectric function model of all the materials building the device layers together with geometrical description of the device. With this set of data, it is possible to calculate the electromagnetic mode structure of the device and the distribution of excited states in the active layers for monochromatic or polychromatic light impinging on the device. This allows calculations of the energy redistribution between layers and gives input to the determination of charge carrier distribution within the device. This, in turn, is a necessary input for models of electrical transport in the device under illumination, to build a full-fledged model of optical processes and electrical transport in PPVDs. The optical processes are the topic of this chapter.

Simulations have sometimes been described as the third cornerstone of physics of equal merit with the traditional pillars of theory and experiment.[1] In simple terms it is the technique of performing experiments, not on the real system which ultimately is the interesting topic, but on its model.[2,3] The model is the result of mapping some aspects of real system — in our case a polymer-based photovoltaic device and its optical behavior — so that the system complexity is decreased to manageable levels but still leaves a model powerful enough to deliver nontrivial results. The mapping heavily depends on the understanding of the processes inside and how well the processes can be described in mathematical language, i.e., physical formulas and in program code, and a valuation and judgment of what is important

and what is superfluous. Today's user-friendly software, where much of the complicated calculations are concealed to the user, makes a computerized simulation the standard choice.

The great benefit with simulation is avoidance of manipulating a set of real-world objects. This saves resources, both time and working efforts, as well as materials as often only very small quantities are available. During some tenths of hours on an ordinary PC, 20,000 different PPVD structures can be defined and simulated, irradiated with artificial solar light consisting of 500 wavelengths and then analyzed with respect to their optical response. This is simply not possible to achieve with experiments. When scanning this large number of structures, it is natural to pick out which in some sense is the best one, and by this entering into the realms of optimization. Through simulation, which exhausts all — within limits — parameter combinations, the classical obstacle in optimization is avoided, namely solving the inverse problem when one starts from a parameter-dependent objective function and goes backwards to the parameter space for the optimal combination.

Real experiments demand planning and thoughtful considerations. Simulation on the other hand gives an unsurpassed opportunity to test casual thoughts and examine innovative alternatives — with an answer within minutes. Finally, by simulation it is possible to reach otherwise inaccessible quantities, exemplified with the calculation of the square modulus of the optical electric field in every point inside the PPVD, or the distribution of excited states within the thin films inside a device.

The de-coupling of the model from the real system is also the source of the weakness of the procedure. Even if simulation has the ability to confirm the experimenter's prejudice, or predict the unforeseen, it must be tested on dummy examples and checked against experiments. To bring in physical justification makes simulation somewhat of an art and something more than brute programming.

In the following we will give an example of how a simulation of a PPVD, a "solar cell," can be done and go into details of assumptions and derivations besides delivering useful results. In general terms the simulation presented is simple and straightforward. It is *static* in that time-dependence is not relevant, and *deterministic* as no variables or processes are modeled as stochastic.

Based on the formalism developed, we are able to calculate the total electromagnetic (EM) field at any point inside the device, taking into account both the primary irradiated light and light reflected in different internal interfaces. In a thin film stack, which indeed is a part of the device, this gives rise to interference. As we simulate polychromatic solar-distributed irradiation, the model will allow us to calculate absorbed energies as absolute values. One of the great advantages of the model is that it offers the opportunity to optimize the structure so that maximum energy is absorbed. The free variables are the layer thicknesses, and by varying them the total reflectance, and the beneficial and nonbeneficial absorption is changed. From this information, an optimal set of thicknesses can be determined, given the materials and their optical properties. It is also possible to resolve the spatial energy dissipation and to construct EM field profiles. This is done both for monochromatic and polychromatic light. Simulation also admits calculation of reflectance and allows estimates of limits of quantum efficiencies.

After a short description of the physics involved in a PPVD, the matrix-based formalism underlying the simulation is presented in detail. Then results follow. These are first demonstrated for monochromatic irradiation and later for polychromatic

solar light. Three types of structures are studied: (1) the cavity, (2) the double layer structure, and (3) the blend layer structure.

In the following, *geometry* will mean a certain choice of thicknesses, *morphology* refers to the structure of materials, preferentially the active layer, and whether it is in one phase or phase separated, *Topology* refers to the same thing but is restricted to the surface.

To simplify our model we avoid some possible complexities. Only normal incoupling of light is considered. Surface roughness is assumed to be so small that interfaces can be approximated by flat ideal surfaces. We assume linear optical behavior. Important aspects of real PPVDs are therefore excluded, i.e., no waveguiding will be discussed. Anisotropy of layers may be found in these materials, but due to uniaxiality and normal incidence the whole complexity of the anisotropy is not seen, as only the ordinary direction modulates the penetrating light. Both of these exclusions prevent us from analyzing the impact of patterning of layers, where diffractive optics can contribute to the absorption features of devices.

5.2. THE SEVEN PROCESSES OF POLYMER PHOTOVOLTAIC DEVICES

To go beyond the simple working principle for photovoltaic devices, "light in–current out," it is fruitful to leave the holistic system picture for the understanding of PPVDs, and divide and *analyze* the performance into seven processes. These are:

- Incoupling of the photon
- Photon absorption
- Exciton formation
- Exciton migration
- Exciton dissociation
- Charge transport
- Charge collection at the electrodes.

The processes will shortly be described below. The first two items in the list are the optical mechanisms of the device. By formulating the total performance into seven steps, it is possible to de-couple the optical and electrical behavior thereby more clearly finding possibilities for enhancing performance and identifying bottlenecks.

The device geometry in PPVDs is typically a multilayer stack of electrodes and absorber–photocurrent generator layers deposited on a common transparent substrate in a sandwich fashion. It may include special electrode buffer layers for adapting electric conditions at interfaces, layers of p-type and n-type organic conductors, and exciton blocking layers. The substrate can easily be 1000 times thicker than the total multilayer structure.

5.2.1. Incoupling of the Photon

Some interface bounds the device from the outside. Typically devices are manufactured such that the substrate, glass — assumed in the model below — or quartz or a polymeric material is the first material the photons encounter. The criterion is that the material should be as transparent as possible for light. The losses due to reflection at air–substrate interfaces should be minimized. Upon normal incidence from one layer to another, the higher the difference between optical refractive

index, the higher the losses. At $n_{\text{substrate}} = n_{\text{glass}} = 1.5$ the reflectance will be $R = 0.04$ and for $n_{\text{substrate}} = 2$, $R = 0.11$. It is important to realize that the device reflectance is not the same as the reflectance of the air–substrate interface, but depends on all layers including substrate and stack. Manipulating the surfaces by suitable patterning such as downward pointing pyramids, globes, or one-dimensional gratings[4] can diminish losses. Antireflection properties can be controlled also by considering the layer ordering, layer thicknesses, and suitable choices of the dielectric functions of the layers. For this, simulation is an invaluable tool. Corrugation of interfaces[5] gives rise to diffraction, which certainly is part of the optics in the device but this theme will not be included in the present simulation. Any redirecting of photons from normal incidence to some degree of coplanarity with the film surface will help absorption as the path length increases, but is likewise excluded from the model.

5.2.2. Photon Absorption

As we define the active layer as the layer where beneficial absorption (for device function) takes place, it is important to focus as much energy as possible to this active layer. The distribution of the optical electrical field, E, is best described in terms of its square modulus, $|E|^2$ as $|E|^2$ is closely related to absorption. At a given point in the device, $|E|^2$ is dependent both on the local dielectric function at that point and on the global properties of device geometry, including the optical properties of the layers and interfaces.

From a materials perspective, it is important to have an absorption coefficient of the active material that matches the solar irradiation. During the years there has been a continuous striving for lowering the band gap of the polymers used.[6]

It should be kept in mind that PPVDs are in the realm of thin film optics. Therefore simple assumptions of Beer–Lambert absorption (given by the following equation) are inadequate.

$$S_{\text{t}} = S_{\text{in}} e^{-\alpha d} \tag{1}$$

where S is power per unit area, α the absorption coefficient, and d the distance calculated from the front interface, and the index "t" refers to transmission. S_{in} should refer to a point immediately inside the interface but is commonly replaced by the power per unit area immediately before the interface, thereby confusing reflectance and absorption. In the inorganic solar cell community, optical modeling based on Equation (1) is common.

5.2.1 and 5.2.2 together describe the optical part of the total PPVD mechanism. For processes 5.2.1 and 5.2.2 a joint efficiency, η_{A}, is formulated as the ratio between the number of absorbed photons in the device and the number of incoming photons to the air–substrate interface.

5.2.3. Exciton Formation

After optical absorption has occurred, the excitation of the organic solid is described in terms of the exciton. The exciton consists of a pair of Coulomb-attracted electrons and holes, is electrically neutral, and can be compared to the Frenkel exciton of solid state physics.

Only a fraction of the incoming photons turn into excitons. One can attribute the exciton formation efficiency η_{EC} with this step. Processes 5.2.2 and 5.2.3 are collectively called photogeneration.

5.2.4. Exciton Migration

In a diffusive three-dimensional migration the exciton moves through the material. A parameter describing this process is the exciton diffusion length, L_D, Typically it is of the order of 5–10 nm but is dependent on the structure of the materials and the dielectric environment.[7]

Excitons have a finite lifetime, and during their diffusion they end their existence via several beneficial as well as disadvantageous decay channels; in a radiative decay, a photon is re-emitted in luminescence, thereby constituting a loss mechanism for a PPVD. All vibronic and thermal decay routes are also loss of energy for PPVDs. The desired path is the transformation of the excitons into free electrons and holes, which is assumed to happen at certain *dissociation sites* where two materials with different electron affinities come into proximity of each other. Conditions for generating charge from excited states may also be found in inhomogeneities in materials, and at interfaces to electrodes, but are typically very inefficient compared to processes of photoinduced charge transfer at junctions between two dissimilar materials, and are therefore neglected here.

From the diffusion length L_D, we define a diffusion zone. This is the part of the device that has the ability to give charge carriers for a photocurrent. The diffusion zone can extend into one or several layers.

5.2.5. Exciton Dissociation

Solar cell dissociation of the exciton into free charge carriers (electron and hole) is the beneficial way of converting the energy emerging from the absorbed photon. At the dissociation site the electron and the hole are separated, free to move, or to move and then be trapped.

Processes counteracting the dissociation are the (geminate) recombination where separated electrons and holes merge back into an exciton, because the field is too weak for separation beyond electrostatic attraction, and nongeminate bimolecular recombination when an electron and a hole generated from different excitons recombines. A mobile hole may also recombine with a trapped electron.

5.2.6. Charge Transport

The free charges must be allowed to reach the electrodes where they constitute the photocurrent from the device.

The location of the dissociation site is important for the extracted photocurrent. Electrons and holes have different mobilities in the material. Trapping into localized states may occur. Irrespective of whether the trapping is permanent or temporary, the efficiency of charge transport is diminished. As the risk for trapping increases with the distance traveled, a thin layer is better than a thick layer, but optical absorption, which is proportional to thickness, is simultaneously reduced.

Recombination of free charge carriers into excitons, and between one trapped and one free carrier, is another loss mechanism.

5.2.7. Charge Collection

Even if an electron or a hole is present close to an electrode, whether they will pass into the outer circuit is not certain. The probability associated with all the barrier penetration mechanisms involved at the interfaces towards the metallic surfaces is a function of geometry, topology, and interface formation.

5.3. ROUTES TO OPTICAL MODELS OF PPVDs

In the literature on modeling of organic photovoltaic devices from Ghosh et al. and forward,[8–10] much of the focus has been on the processes 5.2.4 to 5.2.7. Often less attention is paid to the optics, with photon absorption commonly described as a simple source term in an exciton diffusion equation, or by assuming a Beer–Lambert (Equation (1)) decrease of absorption or production from the front interface. Realistic optical models must include reflection at internal interfaces and the subsequent interference in these thin film structures. Studies of this kind are in demand but not frequent.[7,11–14] Support from the inorganic solar cell literature is scarce as typically layers are thicker with these materials. Systems with both coherent and incoherent light addition has been discussed in a number of studies.[15–21]

Considerations of interference effects in PPVD was done by Halls[22] but best described in his doctoral dissertation.[23] The approach avoids cumbersome calculations because of intensity rather than addition of amplitude. Input parameters are the transmittances through the active layers upstream and downstream, reflectance at the aluminium interface, and thickness and absorption coefficient of the active layer.

One of the first thoroughly worked out studies was by Petterson.[24] In a matrix formalism, internal reflections and interference could be handled for calculating the electrical field at any given point inside the device. This in turn made it possible to calculate the absorbance as identified with the energy dissipation. In this calculation, input parameters were the thicknesses of the layers and the complex dielectric functions of the materials involved.

Peumans et al.[7] followed the same line in a large study mainly devoted to small molecular material (CuPc). Hoppe et al.[13] addressed blended active layers. Their case is the para-phenylene-vinylene derivative MDMO–PPV and [6,6]-phenyl-C_{61}-butyric acid methyl ester (PCBM) by 1:4 wt.%. The connection between model and experimental data is the photocurrent. This is also used by Rostalski and Meissner[14] for a double layer of small molecular materials with calculations based on a slightly different expression for the absorptance. All these four articles also aim for optimizing the performance by finding the right layer thickness combination and in the case of Peumans and Rostalski, and Meissner, experimenting with added layers.

A somewhat different approach to interference modeling was taken by Stübinger.[25] Still if the model was simple it was potent enough to give estimates of the optimal fullerene layer thickness by curve fitting.

It can be noted that the literature does not seem to include examples of two-dimensional models, allowing non-normal angle of incidence. Idealization prevails concerning layer homogeneity, thickness uniformity, and interface sharpness. More elaborate studies of electromagnetic transmission, for example using finite element methods, could be the next step.

5.4. THE MATRIX MODEL

5.4.1. General Assumptions

The primary purpose of the modeling is to find the optical electric field, E, at every point. E will be a complicated function of the dielectric functions and thicknesses of the materials.

Going by the conventional way of building PV devices in a stacked sandwich-like fashion, the structure lends itself to a one-dimensional model. The directions are indicated in Figure 5.1 where $+$ indicates down into the device, and $-$ upstream. The plane of incidence is defined by the plane normal, the incident, and the (specular) reflected ray. By "p", we indicate light with polarization parallel to the plane of incidence and by "s" (from German *senkrecht*) we mean vertical or perpendicular light. It is always possible to decompose light into these two directions. It is sufficient to follow only one ray hitting the surface at a certain point, which is the origin. A Cartesian coordinate system is introduced, $Oxyz$, with x and y in the plane and z into the device, perpendicular to the plane surface. x and y will sometimes be summarized with $\parallel$ and z with $\perp$.

Layers will be numbered starting with 0 for air, 1 for the substrate, and so on. The index of refraction is a complex quantity for which we will use the plus sign convention: $\tilde{n} = n + ik$.

Matrices are intimately related to linear processes. As linearity will be used as an assumption, in a way explained below, together with the inherent one-dimensionality and the separation into $+$ and $-$ direction a matrix formalism gives an effective
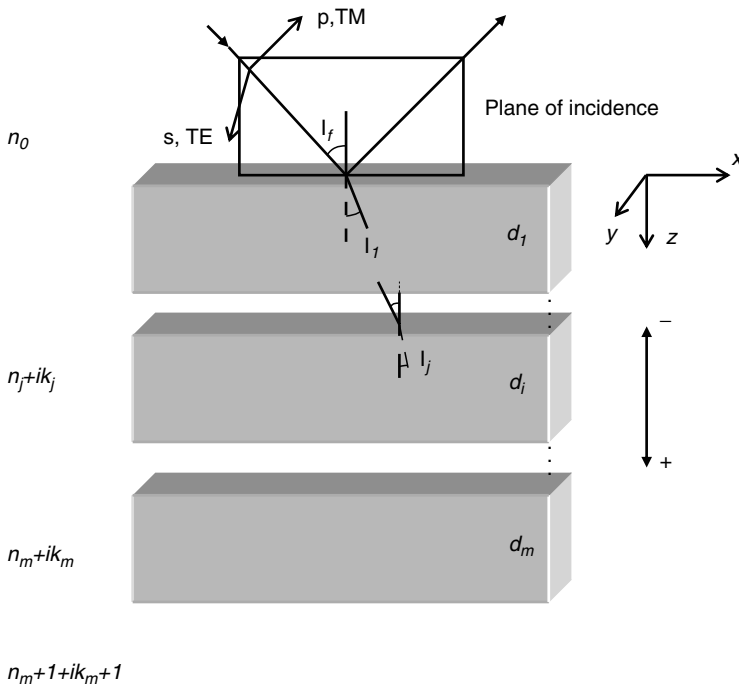

Figure 5.1. Modeling of the stack. Coordinate system is shown with plane of incidence and angle of incidence. j indicates a general layer and m is the last one in the stack. 0 and $m+1$ are semiinfinite.

description. The code is written in Matlab (The MathWorks, Inc), a mathematical software based on matrix manipulations.

We assume layers to be smooth and homogeneous, and interfaces to be parallel. We do not take scattering into account. But we make no assumptions of isotropy. In fact, some of the materials involved are found to be uniaxial anisotropic.

It is necessary for the optical treatment to divide the structure into two parts, a multilayer thin film *stack* and a comparatively much thicker glass *substrate*. Internally in the stack, the light is coherently added using a matrix formalism, as typical layer thicknesses and irradiated wavelengths are of the same order of magnitude. Whenever the millimeter-thick substrate is also taken into account, coherence is lost and irradiances rather than optical field amplitudes must be added.

5.4.2. Derivation — the Stack Model

We start by decomposing the optic electrical field into an upstream and a downstream component

$$E = E^+ + E^- \quad \text{for s or p}$$

For a nonpatterned surface and isotropic or uniaxial anisotropic with optical axis normal to the plane, E, E^+, E^- does not depend on x and y. Therefore we write

$$E(z) = E^+(z) + E^-(z) \tag{2}$$

for each polarisation state, s and p. The indexation with s and p will be omitted in most cases in the following discussion, but is still relevant. For relating two nearby points, z_1 and z_2, we assume linearity

$$E^+(z_1) = M_{11}E^+(z_2) + M_{12}E^-(z_2)$$
$$E(z_1) = M_{21}E^+(z_2) + M_{22}E^-(z_2) \tag{3}$$

Introducing the generalized field vectors $(E^+, E^-)_x^T$ and the scattering matrix, M, consisting of the numbers M_{ij}, $i, j = 1,2$, we comprehend these equations into a single vector–matrix relation

$$\begin{pmatrix} E^+ \\ E^- \end{pmatrix}_{z_1} = M \begin{pmatrix} E^+ \\ E^- \end{pmatrix}_{z_2}$$

The nearby points can be related in either of the two cases; if z_1 and z_2 are in the same layer without any interface in between, we write

$$\begin{pmatrix} E^+ \\ E^- \end{pmatrix}_{z_1} = L \begin{pmatrix} E^+ \\ E^- \end{pmatrix}_{z_2}$$

but if z_1 and z_2 are on opposite side of an interface, just inside the two layers, we write

$$\begin{pmatrix} E^+ \\ E^- \end{pmatrix}_{z_1} = I \begin{pmatrix} E^+ \\ E^- \end{pmatrix}_{z_2}$$

L is denoted as layer matrix and I as interface matrix. For layer j, we write L_j and for the interface between layer i and j, I_{ij}. Thus, for two points z_0 in layer 0 and z_{m+1} in layer $m+1$,

$$M = I_{01}L_1L_{12}L_2L_{23}L_3, \ldots, L_mI_{m,m+1} = \left(\prod_{v=1}^{m} I_{v-1,v}L_v \right) I_{m,m+1} \tag{4}$$

$(E^+, E^-)_0^{\mathrm{T}}$ is the same as $(E_{\mathrm{in}}, E_{\mathrm{refl}})^{\mathrm{T}}$ where 'in' indicates incoming and 'refl' the reflected field amplitude, and for $(E^+, E^-)_{m+1}^{\mathrm{T}}$ we put $(E_{\mathrm{trans}}, 0)^{\mathrm{T}}$.

The Fresnel complex transmission and reflection coefficients then relates the amplitudes as

$$t = \frac{E_{m+1}^+}{E_0^+} \tag{5}$$

$$r = \frac{E_0^-}{E_0^+} \tag{6}$$

Applying (3)

$$\begin{cases} E_0^+ = M_{11} E_{m+1}^+ + 0 \\ E_0^- = M_{21} E_{m+1}^+ + 0 \end{cases} \text{gives} \begin{cases} t = \frac{1}{M_{11}} \\ r = \frac{M_{21}}{M_{11}} \end{cases} \tag{7}$$

It is now possible to determine I_{ij} (Figure 5.2(a)). The relation

$$\begin{pmatrix} E^+ \\ E^- \end{pmatrix} = \begin{pmatrix} I_{11} & I_{12} \\ I_{21} & I_{22} \end{pmatrix} \begin{pmatrix} E^+ \\ E^- \end{pmatrix}_j$$

is true for all $(E^+, E^-)^{\mathrm{T}}$ in particular for the situation in Figure 5.2(b): $E_j^+ = t_{ij} E_i$, $E_j^- = 0$, and $E_i = r_{ij} E_i^+$ which gives I_{11} and I_{21} and for the situation in Figure 5.2(c): $E_j^+ = r_{ji} E_j^-$, $E_i^+ = 0$, and $E_i^- = t_{ji} E_j^-$. Fresnel formulae give $r_{ij} = -r_{ji}$ and

$$t_{ij} = \frac{1 - r_{ji}^2}{t_{ji}}$$

from which it is possible to derive the complete I_{ij}-matrix:

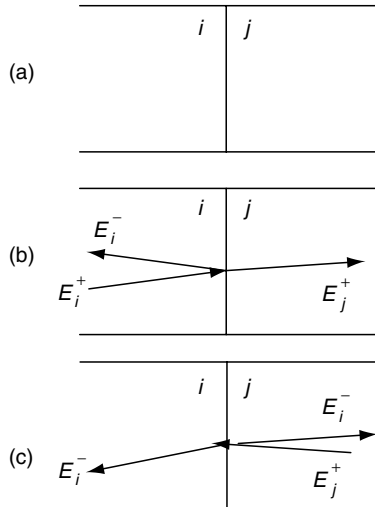$$I_{ij} = \frac{1}{t_{ij}} \begin{pmatrix} 1 & r_{ij} \\ r_{ij} & 1 \end{pmatrix} \tag{8}$$

Figure 5.2. (a) Derivation of the I-matrix, i and j are two adjacent layers in the stack. (b) A ray from the left, which gives reflection and refraction. (c) A ray from the right, which is reflected and refracted.

Via Fresnel formulae for r_{ij} and t_{ij}, I_{ij} can be expressed in the indices of refraction and angle of incidence.

We now turn to L_j. For a passage through layer j (see Figure 5.3) of thickness d, index of refraction n, angle of refraction ϕ, and the phase difference β

$$\beta_j = \frac{2\pi d}{\lambda} n_j \cos \phi_1 = \xi_j d$$

where

$$\xi_j = \frac{2\pi}{\lambda} n_j \cos \phi_1.$$

Then $E_{d=0}^+ = e^{-i\beta} E_d^+$ and $E_{d=0}^- = e^{+i\beta} E_d^-$ which gives

$$L_j = \begin{pmatrix} e^{-i\beta_j} & 0 \\ 0 & e^{i\beta_j} \end{pmatrix} \tag{9}$$

Having both L_j and I_{ij} we are able to start to dwell upon the E-field in layer j.

The environment around layer j is partitioned into an upstream system indicated with $'$ and a downstream system indicated with $''$ (Figure 5.4(a)),
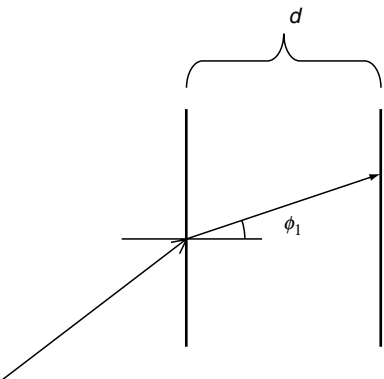
$$M = M_j' L_j M_j''$$

Figure 5.3. Deriving β. A ray passes through a medium of thickness d.
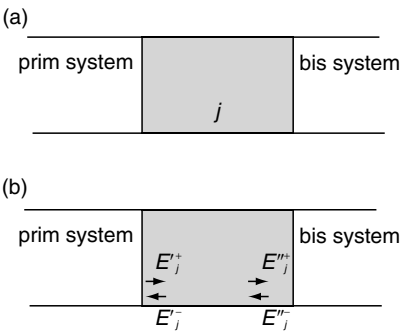

Figure 5.4. (a) Focusing on a certain layer j in the stack. The environment is indicated $'$ and $''$ respectively. (b) Output and input to layer j in the form of electrical field amplitudes. The arrows indicate the direction of propagation, not the field amplitudes.

where

$$M'_j = \left(\prod_{v=1}^{j-1} I_{v-1,v} L_v\right) I_{j-1,j}$$

$$M''_j = \left(\prod_{v=j+1}^{m} I_{v-1,v} L_v\right) I_{m,m+1}$$

The upstream and downstream systems have their own reflection and transmission coefficients for which bis quantities follow:

$$t''_j = \frac{1}{M''_{j,11}}$$

$$r''_j = \frac{M''_{j,21}}{M''_{j,11}} \tag{10}$$

derived in the same manner as (7).

It will turn out to be efficient to introduce certain transfer coefficients that couples between layer j and the incoming light:

$$t^+_j = \frac{E^+_j}{E^+_0} \tag{11}$$

$$t^-_j = \frac{E^-_j}{E^+_0} \tag{12}$$

Expressions can be derived with these transfer coefficients. For the upstream system

$$\begin{pmatrix} E^+_0 \\ E^-_0 \end{pmatrix} = \begin{pmatrix} M'_{j,11} & M'_{j,12} \\ M'_{j,21} & M'_{j,22} \end{pmatrix} \begin{pmatrix} E'^+_j \\ E'^-_j \end{pmatrix}$$

which gives

$$E^+_0 = M'_{j,11} E'^+_j + M'_{j,12} E'^-_j \tag{13}$$

The downstream system

$$\begin{pmatrix} E''^+_j \\ E''^-_j \end{pmatrix} = \begin{pmatrix} M''_{j,11} & M''_{j,12} \\ M''_{j,21} & M''_{j,22} \end{pmatrix} \begin{pmatrix} E'^+_{m+1} \\ 0 \end{pmatrix}$$

contains elements related such as

$$r''_j = \frac{M''_{j,21}}{M''_{j,11}} = \frac{E''^-_j}{E''^+_j}$$

Applying (9) gives

$$\begin{pmatrix} E'^+_j \\ E'^-_j \end{pmatrix} = \begin{pmatrix} e^{-i\beta_j} & 0 \\ 0 & e^{i\beta_j} \end{pmatrix} \begin{pmatrix} E''^+_j \\ E''^-_j \end{pmatrix}$$

i.e.,

$$r''_j = \frac{E''^-_j}{E''^+_j} = \frac{E'^-_j e^{-i\beta_j}}{E'^+_j e^{i\beta_j}} = -\frac{1}{r'_j} e^{-2i\beta_j}$$

Divide (13) by $E_j'^+$. Then

$$t_j^+ = \frac{1}{M_{j,11}' + M_{j,12}' r_j'' e^{i2\beta_j}}$$ (14)

and by dividing (13) with $E_j'^-$, it is easy to show that

$$t_j^- = t_j^+ r_j'' e^{i2\beta_j}$$ (15)

We are now ready for expressing the E-field inside layer j. From $E_j(z) = E_j^+(z) + E_j^-(z)$ we use (11), (12), (14), and (15), and finally expressing all coefficients in terms of matrix elements,

$$E_j(z) = \frac{M_{j,11}'' e^{i\xi_j(z-d_j)} + M_{j,21}'' e^{i\xi_j(d_j-z)}}{M_{j,11}' M_{j,11}'' e^{-i\xi_j d_j} + M_{j,12}' M_{j,11}'' e^{i\xi_j d_j}} E_0^+$$ (16)

where z belongs to layer j.

Based on the Poynting theorem,[26–28] that can be interpreted as a statement of conservation of energy,

$$Q(z) = \langle -\nabla \cdot \mathbf{S} \rangle$$ (17)

where Q is the (time average) energy flow dissipation per time unit at the point z, $\langle\ \rangle$ indicates time average and $\mathbf{S}$ is the Poynting vector,

$$\mathbf{S} = \mathbf{E} \times \mathbf{H}$$

Because time averaging of a product of $\tilde{A} = A_0 e^{i(kx-wt)}$ and $\mathbf{B} = \mathbf{B}_0\, e^{i(kx-wt)}$ can[28] be performed as $\frac{1}{2}\mathrm{Re}(\tilde{A}\tilde{B}^*)$ and

$$-\nabla \cdot \mathbf{S} = \left(\mathbf{H}\frac{\partial \mathbf{B}}{\partial t} + \mathbf{E}\frac{\partial \mathbf{D}}{\partial t} \right)$$

using Maxwell equations, one can show that

$$Q(z) = \frac{1}{2} c\varepsilon_0 \alpha n |\mathbf{E}(z)|^2$$ (18)

Q has the unit $\mathrm{W/(m^2\, nm)}$ where it is indicated that z, the distance is measured in nm. c is speed of light, 3.00×10^8 m/s, ε_0 is permittivity of vacuum, 8.85×10^{-12} F/m, n is the real index of refraction, α is the absorption coefficient, $\alpha = 4\pi k/\lambda$ with $\tilde{n} = n + ik$ and λ is the vacuum wavelength; and $\mathbf{E}(z)$ is the total electrical optical field at the point z. All parameters are for the layer under consideration. The factor 1/2 is due to averaging of the rapid frequency variation, ca. 10^{14} Hz, in the optical field. Q is a discontinuous function of z, and Q at the points corresponding to the interfaces is not well defined.

When comparing our calculations with experiments, we will use the accumulated dissipation Q from an interval of z,

$$\int_{z\in \text{interval}} Q(z)\mathrm{d}z.$$

These Qs will be indexed as Q_{zone} and $Q_{\text{zonedouble}}$ as explained later.

For a given layer j in the stack, the absorptance A_j is related to Q as

$$A_j = \frac{1}{S_0} \int\limits_{z \in \text{layer } j} Q(z)\mathrm{d}z \tag{19}$$

where S_0 is the irradiance from air for a given wavelength.

5.4.3. Taking Into Account the Substrate

$E(z)$ is dependent on the incoming field to the stack. This is not the same as that coming to the glass substrate from air, but is moderated due to reflection at the air–glass interface and multiple reflection at glass–air interface (Figure 5.5). Light from the left is entering with a general angle of incidence of θ. Reflection occurs in the air–glass interface with some of the light reflected and some transmitted to the stack. Another division between reflected and transmitted light takes place at this interface. The reflected part goes back towards the glass–air interface, where some part of the reflected light re-enters into air and adds with the light reflected only once and some part of it turns back to the stack, and so on.

Using the Poynting vector, the irradiance in air B is

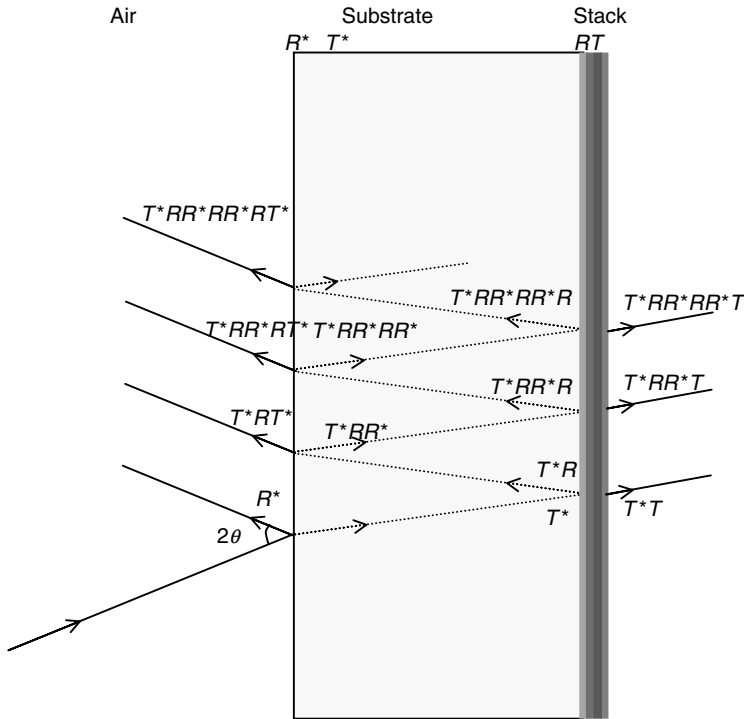$$B = \frac{1}{2} c \varepsilon_0 |\mathbf{E}_0|^2$$

Figure 5.5. Optics in the structure. R represents reflectances and T transmittances. Star (*)-marked quantities refer to the glass substrate, unmarked to the stack. The derivation was done generally keeping a finite T although it is later assumed that T is zero due to thick enough aluminium. The angle if incidence is θ. Normal incidence is used throughout the study.

For an optical description of the diode, we cut the device into two optical elements — the *stack* consisting of the multilayer of thin films, indium tin oxide, ITO, poly(3,4-ethylene dioxythiophene)poly(4-styrenesulfonate), polymer blend, and the other layers, and the *substrate*, which in our case is glass. Typically the thicknesses for the stack layers are less than the irradiated wavelength ($\approx 0.5\,\mu m$), whereas the distance between the stack and the air–substrate interface is of the order of millimeters. This makes it necessary to add light coherently inside the stack and incoherently, using irradiances, when the substrate is involved.

Let the air–glass interface be characterized by a reflectance R^*. The substrate has a transmittance T^*. The reflectance and transmittance for the stack are R and T, respectively. All these quantities can be calculated from the complex indices of refraction of the materials and the different layer thicknesses through Fresnel equations. For normal incidence from a material i to j, the reflectance is

$$\text{reflectance} = \frac{(n_j - n_i)^2 + (k_j + k_i)^2}{(n_j + n_i)^2 + (k_j + k_i)^2} \tag{20}$$

The total transmittance for the whole structure (Figure 5.5) is calculated by adding energy (irradiance) quantities. Then

$$T_{\text{tot}} = T^* \left(\sum_{i=0}^{\infty} (RR^*)^i \right) T = T^* \frac{1}{1 - RR^*} T = \frac{T^* T}{1 - RR^*}$$

For the total reflectance,

$$R_{\text{tot}} = R^* + T^* \left(\sum_{i=0}^{\infty} (R^* R)^i \right) RT^* = R^* + T^* \frac{1}{1 - RR^*} RT^*$$

Explicitly including absence of absorption in the substrate i.e., $1 = R^* + T^*$ we reach

$$T_{\text{tot}} = \frac{(1 - R^*)T}{1 - RR^*} \tag{21}$$

and

$$R_{\text{tot}} = R^* + \frac{(1 - R^*)(1 - R^*)}{1 - RR^*} R = \frac{R^* + R - 2R^* R}{1 - RR^*} \tag{22}$$

The irradiance to the stack is

$$T \left(\sum_{i=0}^{\infty} (R * R)^i \right) B = T * \frac{1}{1 - RR*} B = \frac{1 - R*}{1 - RR*} B$$

Writing this as $\frac{1}{2} c \varepsilon_0 n_g |E_{o,\,g}|^2$ (where the subscript g indicates a quantity in glass), one reaches

$$|E_{o,g}|^2 = \frac{2(1 - R^*)B}{\varepsilon_0 c n_g (1 - RR^*)}$$

This is the square modulus amplitude that has to be used as input to the Q calculation. Compared to a stack in air the expression is modified with the factor

$$\frac{(1 - R^*)}{n_g (1 - RR^*)}.$$

Under the assumption of zero stack transmittance, fully transmitting glass and no scattering effects,

$$1 = R_{\text{tot}} + \sum_j A_j.$$

5.4.4. Solar Spectrum

A solar cell is to be exposed to polychromatic solar light rather than monochromatic. The simplest approximation is perhaps to treat the sun as a blackbody radiator. Modulating the peak position to 515 nm and the peak value (1.5 W/m^2) to resemble Air Mass 1.5 standard[29] (AM1.5) we introduce the quantity B proportional to the Planck expression

$$B \propto \frac{2hc^2}{\lambda^5} \frac{1}{e^{hc/\lambda kT} - 1} \tag{23}$$

with $T = 5630$ K (equivalent solar blackbody temperature) and the Planck constant $h = 6.63 \times 10^{-34}$ Js. λ is the vacuum wavelength.

We will consider the wavelength interval 300 to 800 nm. The total amount of irradiated power is

$$S_0 = \int_{\lambda = 300\,\text{nm}}^{800} B(\lambda)\mathrm{d}\lambda = 632 \text{ W/m}^2 \tag{24}$$

with our AM1.5 approximation. As a comparison, taking a more extended range,

$$S_0 = \int_{\lambda = 300\,\text{nm}}^{2500} B(\lambda)\mathrm{d}\lambda$$

this value would be 1131 W/m^2, closer to the standard,[29] 952 W/m^2.

5.4.5. Efficiencies

As absorptances are additive $A = \sum_{\text{all}j} A_j$ where we single out A_a, the absorptance in the active layer with the definition

$$\eta_{A_a} = A_a = \frac{\text{number of photons absorbed in active layer}}{\text{number of incoming photons to the structure}} \tag{25}$$

The external quantum efficiency η_{EQE} is experimentally determined, and is commonly defined as the number of electrons generated in the photovoltaic device (at short circuit) divided by the number of incoming photons to the structure. It is measured for monochromatic light. Of the seven processes mentioned in the introduction, some processes could be attributed with certain efficiency. We choose to single out only η_A, the ratio between the number of absorbed photons in the device and the number of incoming photons, but amalgamate the processes 5.2.3 to 5.2.7 in a geometry, topology, and interface formation dependent function. This function is identified with η_{IQE}, the internal quantum efficiency, a quantity cleared from reflection:

$$\eta_{\text{IQE}} = \frac{\text{number of electrons in an outer circuit}}{\text{number of photons absorbed}} \tag{26}$$

Then

$$\eta_{EQE} = \eta_{IQE}\eta_A \tag{27}$$

or

$$\eta_{IQE} = \frac{\eta_{EQE}}{\eta_A} \tag{28}$$

As the number of photons absorbed is a lower number than the number of incident photons $\eta_{IQE} \geq \eta_{EQE}$. Thus η_A is an upper limit for η_{EQE}. We identify η_A with A.

From $1 = R_{tot} + A + T_{tot}$ using additivity of A and assuming $T_{tot} = 0$ one gets $1 = R_{tot} + A_w + A_a$ from which η_{aap}, the active layer absorption part, is defined: $\eta_{aap} = A_a/(A_w + A_a) = A_a/A$. A_w is absorptance in parts of the device that do not generate photocurrent (electrodes, buffer layers). A measure of how efficient a certain layer is to transform a photon to charge carrier is η_{IQEj}, the layerwise internal quantum efficiency (in principle we only consider the active one(s)):

$$\eta_{IQE,j} = \frac{\text{number of electrons in an outer circuit coming from } j}{\text{number of photons absorbed in } j} \tag{29}$$

From the very definition of *active layer*, the numerator is the same as that of (26) when $j = a$. The denominator is A_a times the number of incoming photons to the structure giving

$$\eta_{IQE,a} = \frac{\eta_A \eta_{IQE}}{A_a} = \frac{\eta_{IQE}}{\eta_{aap}} \tag{30}$$

One sees that η_{aap} is an upper limit for η_{IQE}. Because A_a is less than $A = \eta_A$, $\eta_{IQEa} \geq \eta_{IQE}$.

Finally, the optical power efficiency, η_P, is a energy measure more relevant to device performance, and possible to define both for monochromatic and polychromatic illumination, but used here for the case of simulated solar light:

$$\eta_P = \frac{\text{absorbed optical power}}{\text{irradiated optical power}} \tag{31}$$

5.5. SIMULATIONS AND RESULTS

The theory is now to be used for analyzing photodevices. Three types are to be encountered: (1) the cavity, (2) the double layer structure, and (3) the blend layer structure (Figure 5.6).

1. The cavity is the simplest structure consisting only of four layers: a substrate, a semitransparent electrode material, a polymer, and a mirror of aluminum. For this structure we just treat the *E*-field inside.
2. The double layer structure is a photodiode consisting of a polymer, in this case a copolymer containing polyfluorene. The class of polyfluorenes has evoked some interest as the active layer in recent time.[30–32] As the name indicates (*fluor*enes giving *fluor*escence), they were first noticed for their eminent luminescent properties[33,34] and have found an extensive use in light-emitting diodes. The copolymer is poly(2,7-(9,9-dioctyl-fluorene)-*alt*-5,5-(4′,7′-di-2-thienyl-2′,1′,3′-benzothiadiazole))[DiO-PFDTBT]. For a review, see Chapter 17 (Reference 35). For enhanced
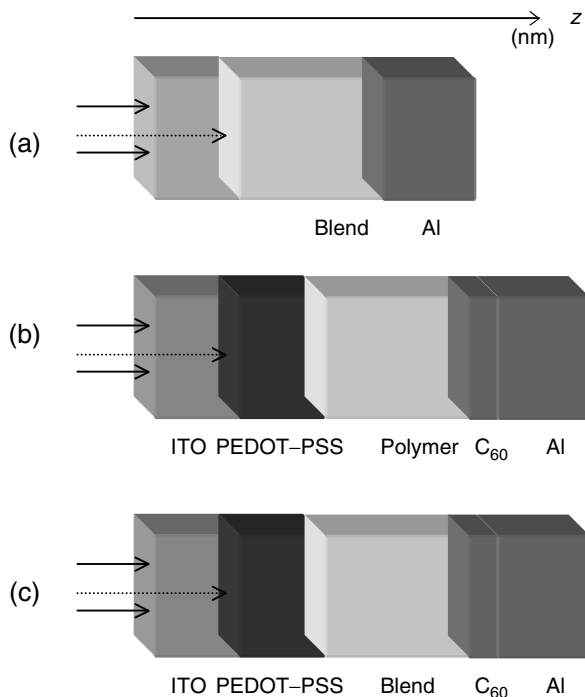
Figure 5.6. The structures assumed for the simulation. Interfaces are assumed to be sharp and layers to be homogeneous. Note that z is calculated from the point where the glass meets the thin film layers and have the unit nm. The glass substrate is many times thicker than any layer in the stack. (a) The cavity consist of only four layers; a substrate (not shown), a semitransparent mirror material, a polymer, and a mirror of aluminum. (b) The double layer structure (d_{ITO}, $d_{PEDOT-PSS}$, $d_{polymer}$, $d_{C_{60}}$) nm. (c) The blend layer structure (d_{ITO}, $d_{PEDOT-PSS}$, d_{blend}, $d_{C_{60}}$) nm.
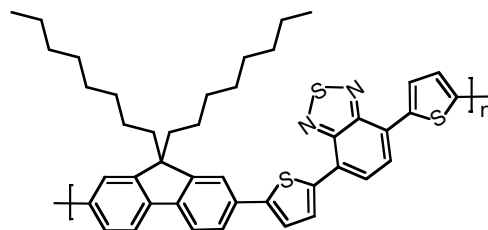
performance, an acceptor-acting layer of C_{60} is added close to the active one. This has the double purpose of both transporting the electrons and, at the interface towards the polymer, providing sites for exciton dissociation. Optical simulation of the double layer structure is presented in Reference 12.

3. The blend layer structure has a blend of DiO-PFDTBT with the fullerene derivative PCBM in the weight proportions 1:4 as the central layer. Added to this is a pure fullerene layer. The blend layer structure and its optical simulation is found in Reference 36.
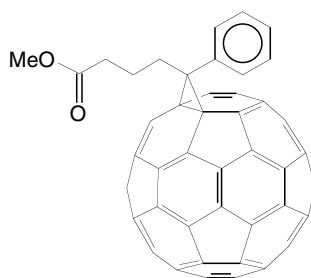
Chemical formulas of the substances are shown in Figure 5.7.

Double layer and blend layer photodevices have different extensions for their diffusion zones. In the double layer structure only a part close to the polymer–C_{60} interface constitutes the diffusion zone. Typically the exciton diffusion length is $10 \, nm$[7,37,38] from which we created a diffusion zone of 10 nm into the polymer counted from the interface but also included 10 nm in the C_{60} layer.
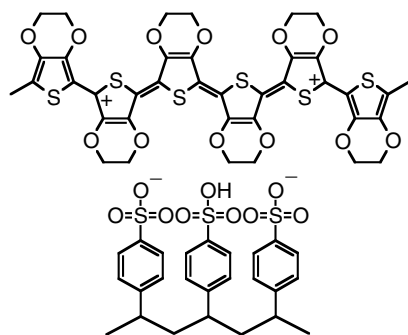
For the blend layer structure, it is assumed that the whole of the blend layer contributes to the photocurrent. This layer is where the bulk heterojunction is

(1)

(2)

(3)

Figure 5.7. Chemical formulas for the constituents in the structures: (**1**) is poly(2,7-(9,9-dioctyl-fluorene)-*alt*-5,5-(4′,7′-di-2-thienyl-2′,1′,3′-benzothiadiazole)) [DiO-PFDTBT], an alternating polyfluorene copolymer, (**2**) is the fullerene derivative [6,6]-phenyl-C_{61}-butyric acid methyl ester (PCBM), (**3**) is poly(3,4-ethylenedioxythiphene)–poly(4-styrenesulfonate) [PEDOT–PSS].

formed, and we focus our attention on this. But we also include the possibility of a layer of C_{60} on top of the blend in some of these calculations.

The criterion for optimization is then to maximize the energy absorption in the diffusion zone.

The input to the calculation is

Dielectric functions for the layers
Layer thicknesses
Diffusion length.

where the dielectric functions for the DiO-PFDTBT is extracted by spectroscopic ellipsometry[12] and is found in Figure 5.8. The same method was used for deriving the $\tilde{\varepsilon}$ for the blend[36] (Figure 5.9). Other material data were taken from previous measurements[12,39] or literature.[40,41] The properties of ITO can vary depending on the manufacturing protocol. We used values previously measured in our group which also agreed with literature findings.[41]

We start by discussing the monochromatic case and then turn to polychromatic irradiation.
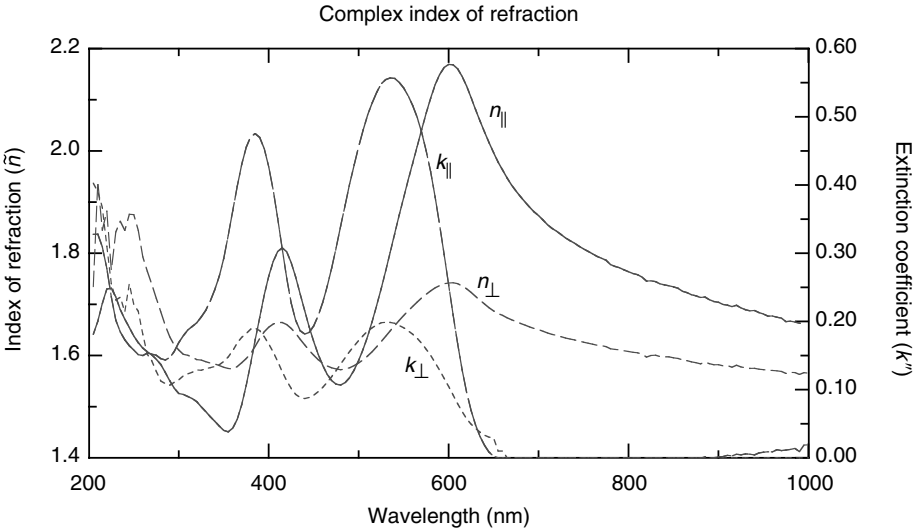

Figure 5.8. $\tilde{n}$ for (**1**) as extracted from spectroscopic ellipsometry. Note that the material is anisotropic. (From N.-K. Persson, M. Schubert, and O. Inganäs. *Solar Energy Materials and Solar Cells*, **83**(2–3), 169–186, 2004. With permission.)
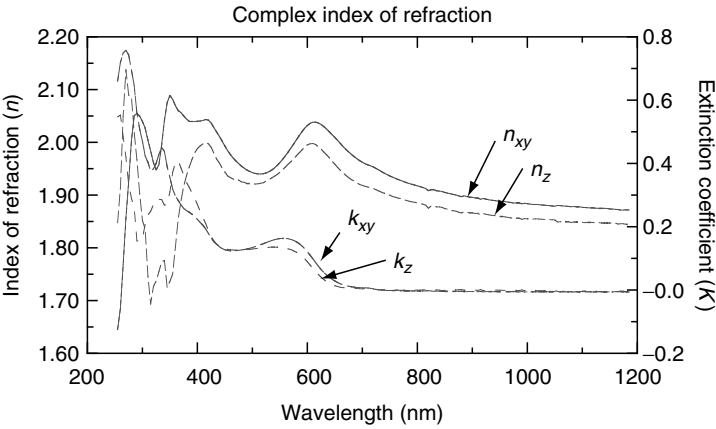

Figure 5.9. $n(\lambda)$ and $k(\lambda)$ for the blend of 4:1 weight ratio PCBM and the copolymer DiO-PFDTBT from ellipsometric investigation in the wavelength interval 240 to 1200 nm. Note that the material is anisotropic. xy is parallel to the surface plane (ordinary direction) and z is normal to the sample plane (extraordinary).

5.5.1. Simulation of the Optical Electric Field Inside the Device

It is appropriate to start with discussion of monochromatic irradiation. The first case to study is the optic electric field distribution inside a simple device, in this case a cavity (Figure 5.10). Normal incidence is assumed.

$|E(z)|^2$ is continuous at the layer interfaces. The high wavelengths 700 and 800 nm create a standing wave behavior as the polymer is not absorbing. The others show different behavior. What is common is the marked undulation. Reflection and interference are indeed marked features. We note that it is possible to choose the illumination wavelength in order to focus the **E**-field to certain positions inside the film.

5.5.2. Q-Profile for Different Wavelengths

Calculating the distribution of the **E**-field using the formalism is only the first step. The time-averaged energy flow dissipation per time unit at the point z is a more interesting quantity as it describes the absorption, and acts like a source term for the exciton production. For the case of structure c, the spatially resolved absorption profile, $Q(z)$, for a certain structure (d_{ITO}, $d_{PEDOT-PSS}$, d_{blend}, $d_{C_{60}}$) is shown in Figure 5.11 for three different wavelengths. Discontinuity at the layer interfaces is seen caused by the sharp change of α and n when going between the materials. The profiles are very different depending on the wavelength. For $\lambda = 300$ nm, the behavior in the blend layer ($z = 140$ to 350 nm) is almost Beer–Lambert-like with only a small superimposed undulation. This is due to the high absorption coefficient. For $\lambda = 550$ nm, the situation is very different.
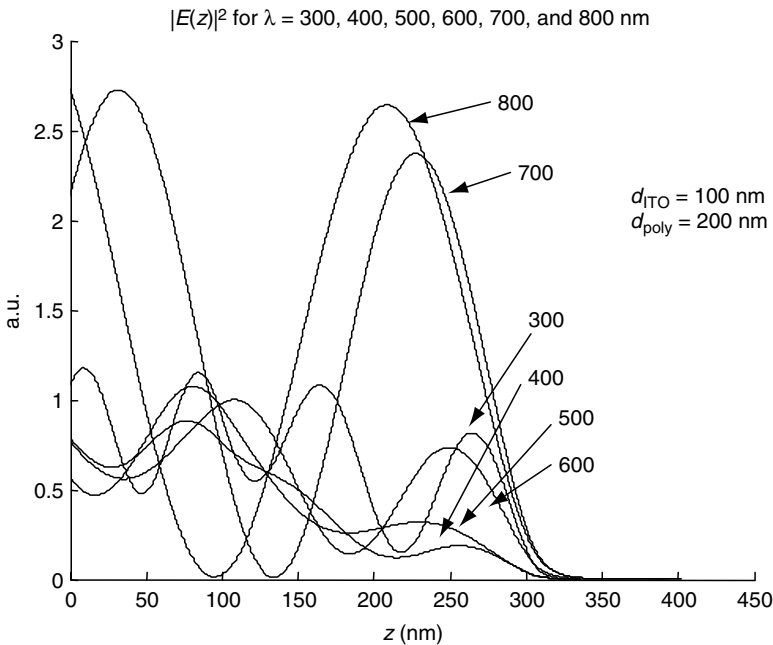

Figure 5.10. The cavity. The distribution of square modulus of electric field for different wavelengths. The geometry is $d_{ITO} = 100$ nm, $d_{polymer} = 200$ nm and aluminum.

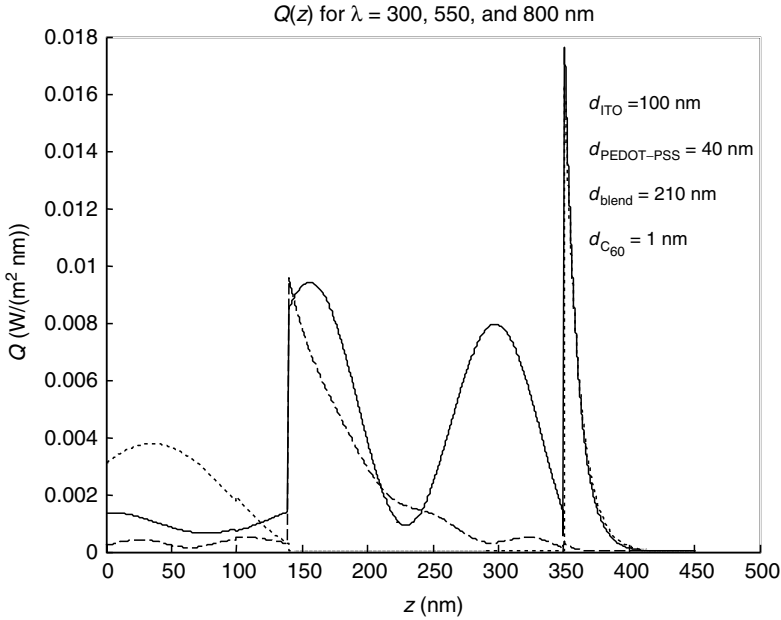**Figure 5.11.** $Q(z)$ for the geometry $d_{ITO} = 100$ nm, $d_{PEDOT-PSS} = 40$ nm, $d_{blend} = 210$ nm, and $d_{C_{60}} = 1$ nm. Irradiated wavelengths are 300 nm, (---) 550 nm (——), and 800 nm ($\cdots\cdots$). As follows from the optimization part, this set corresponds to the optimal geometry for structure c.

Now reflectance in the aluminum and interference with a standing wave behavior is established. Two major peaks inside the blend are seen at $z = 160$ and 300 nm. A small amount of photons are absorbed in the middle of the blend film. $\lambda = 800$ nm is not absorbed at all in the blend. In all three cases, the field is quickly (within 55 nm) diminished in aluminum.

5.5.3. Q-Profile for Different Thicknesses, Monochromatic Illumination

In Figure 5.12, the calculations in 5.5.2 are repeated with only a change of d_{blend} from 210 to 100 nm. The profiles are different from each other but also different compared with profiles shown in Figure 5.11. The blend layer is now so thin that the Beer–Lambert behavior for $\lambda = 300$ nm is lost and $\lambda = 550$ nm now gives a peak in the middle of the blend layer.

5.5.4. Polychromatic Q-Profile

From monochromatic irradiation, the next step is irradiation with polychromatic light. In Figure 5.13, $Q(z)$ is summed over all wavelengths in the interval from 300 to 800 nm. An undulating curve with two hills is seen. This may be compared with the profile for a different blend thickness (Figure 5.14), with the major part of absorption in the middle of the blend layer. The Q distribution is indeed dependent on the geometry. In both cases, the density of excited states is not constant throughout the blend layer.
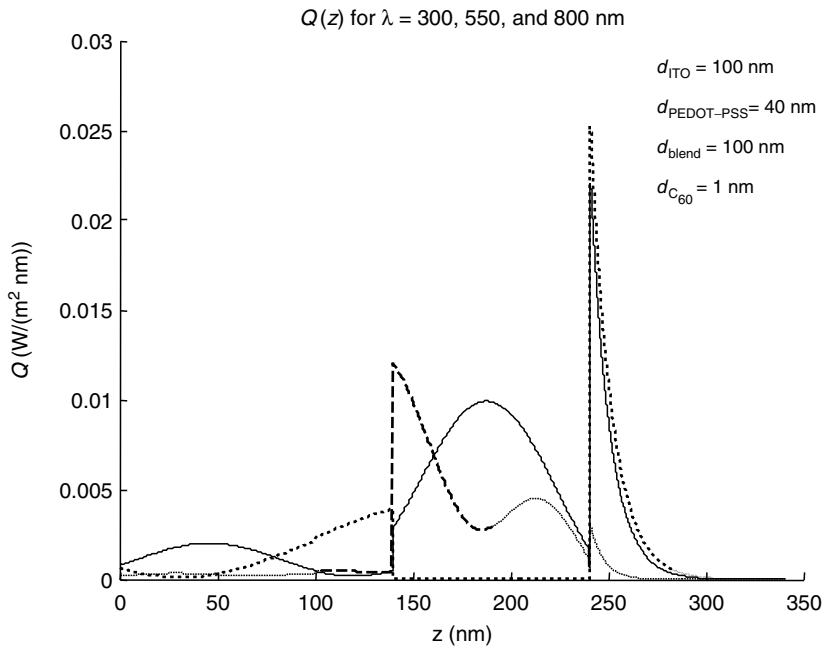
Figure 5.12. $Q(z)$ for the geometry $d_{ITO} = 100\,\text{nm}$, $d_{PEDOT-PSS} = 40\,\text{nm}$, $d_{blend} = 100\,\text{nm}$ and $d_{C_{60}} = 1\,\text{nm}$. Irradiated wavelengths are 300 nm, (---) 550 nm (——) and 800 nm (······) for structure 3.

Figure 5.13. Sum of $Q(z)$ for $\lambda = [300,800]$. The structure (c) is $(d_{ITO}, d_{PEDOT-PSS}, d_{blend}, d_{C_{60}}) = (100, 40, 210, 1)\,\text{nm}$.
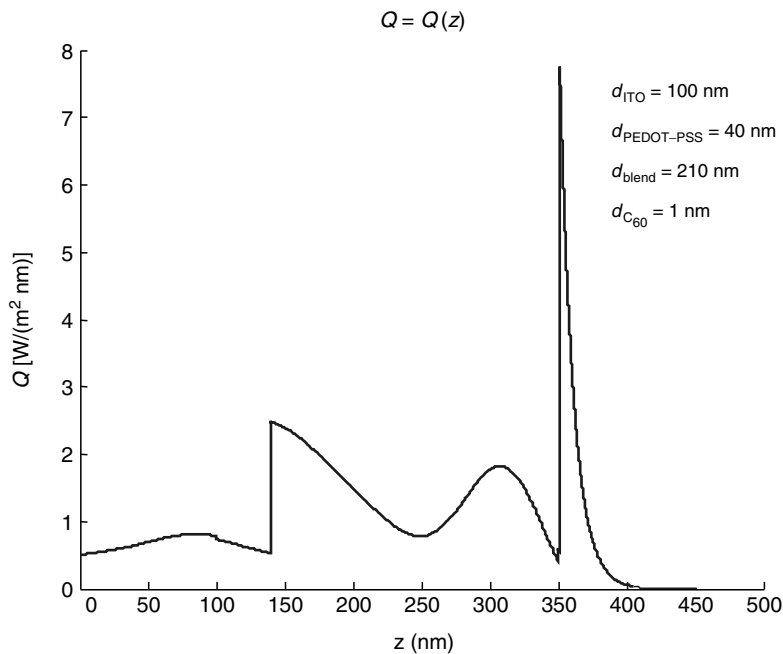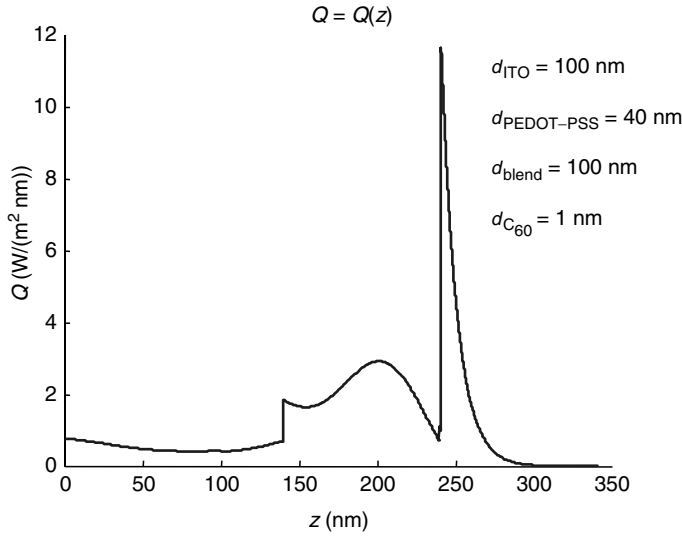
Figure 5.14. Sum of $Q(z)$ for $\lambda = [300,800]$. Structure c. The structure is $(d_{\text{ITO}}, d_{\text{PEDOT–PSS}}, d_{\text{blend}}, d_{C_{60}}) = (100, 40, 100, 1)$ nm.

5.5.5. Device Optimization

The criterion for optimization is to maximize the energy absorption in the diffusion zone. We can then formulate functional relationships such as (suppressing n-dependence)

$$Q_{\text{zone}} = Q_{\text{zone}}(d_{\text{polymer or blend}}, d_{C_{60}}, d_{\text{PEDOT–PSS}}, d_{\text{ITO}}) \qquad (32)$$

with a diffusion zone in the polymer or blend only and $Q_{\text{zonedouble}}$ with an extended zone into C_{60}.

As the diffusion zone in the double layer and the blend layer structures are different, we discuss them separately.

5.5.5.1. Optimizing the Double Layer Structure

As Q_{zone} is a function of many variables, only projections are possible to illustrate, as done in Figure 5.15. In this figure, Q_{zone} as a function of d_{polymer} and $d_{C_{60}}$ for a certain choice of PEDOT–PSS and ITO thicknesses is shown. The ranges of thicknesses are broad, giving us the necessary overview in order to try to find the global maximum. The pictures also illustrate the modest complexity of Q_{zone}.

Details of the optimization of structure 2 can be found elsewhere.[12] In short, an area of high Q_{zone} values can be identified. With respect to the C_{60}-layer, this occurs for values around 50 nm. With respect to the PEDOT–PSS-layer, values around 100 nm are optimal, which agrees with the value used experimentally.[42] The best ITO-thicknesses are those in the interval 70 to 120 nm.

We note that our assumption of a definite 10-nm dissociation zone gives the result that the polymer layer should be as thin as possible. In fact, only counting absorption in the polymer as beneficial and not including parts of PEDOT–PSS in the dissociation zone shows that Q_{zone} decreases if d_{polymer} is less than 10 nm (Figure 5.15). Thus a suitable polymer thickness corresponds to the dissociation zone width. The very value of 10 nm is just an approximate
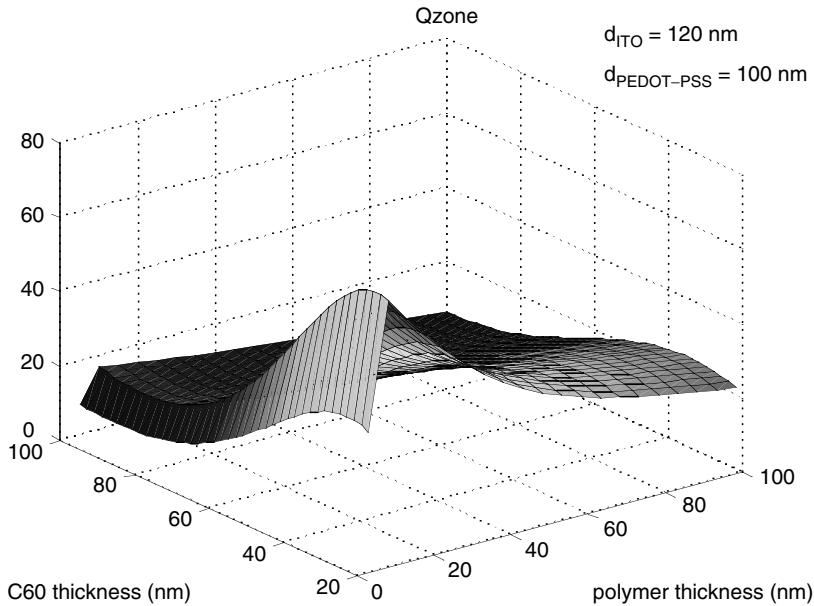
Figure 5.15. Q_{zone} as a function of d_{polymer} and $d_{\mathrm{C_{60}}}$ for structure b. The thickness of PEDOT–PSS is 100 nm and that of ITO 120 nm. Arbitrary values on the ordinate. (From N.-K. Persson, M. Schubert, and O. Inganäs. *Solar Energy Materials and Solar Cells*, **83**(2–3): 169–186 (2004). With permission.)

estimate taken from the literature and should not be given too much emphasis. Other values could have been applied or a probability distribution with a tail further down in the polymer been implemented. However, our simulations point towards the conclusion that extra polymeric material in excess of filling the dissociation zone do not tune the optical electric field into something beneficial for the performance.

To summarize; one example of a thickness combination of the materials studied that gives a high Q_{zone} for structure b is ITO (120 nm), PEDOT–PSS (100 nm), polymer equal to the exciton diffusion length, and C_{60} (50 nm). Of course, this set of optimal values comes from optimization restricted to the optical processes only.

5.5.5.2. Optimizing the Blend Layer Structure

If we now turn to the blend layer structure we take, as was said above, the diffusion zone, Z, to be the whole of the blend layer and 10 nm into C_{60}. The absorbed power per unit area, the integrated Q, which we here call $Q_{\mathrm{zonedouble}} = \int_{x \in Z} Q(z) \mathrm{d}z$ is again calculated for each structure. Optimization is done by varying the thickness of the layers in the range $d_{\mathrm{ITO}} \in \{70,110,150\}$, $d_{\mathrm{PEDOT–PSS}} \in \{40,60,\cdots,120\}$, $d_{\mathrm{blend}} \in \{5,20,\cdots,290\}$, $d_{\mathrm{C_{60}}} \in \{70,110,150\}$. In Figure 5.16, $Q_{\mathrm{zonedouble}}$ is presented as a function of d_{blend} and $d_{\mathrm{C_{60}}}$ for two fixed values of d_{ITO} and $d_{\mathrm{PEDOT–PSS}}$. Note that energies here are given in terms of absolute values (W/m^2). The overall trend is that $Q_{\mathrm{zonedouble}}$ is increasing for increasing d_{blend} and $d_{\mathrm{C_{60}}}$. But some small features are seen on the surface. A faint local maximum of approximately 240 W/m^2 exists around
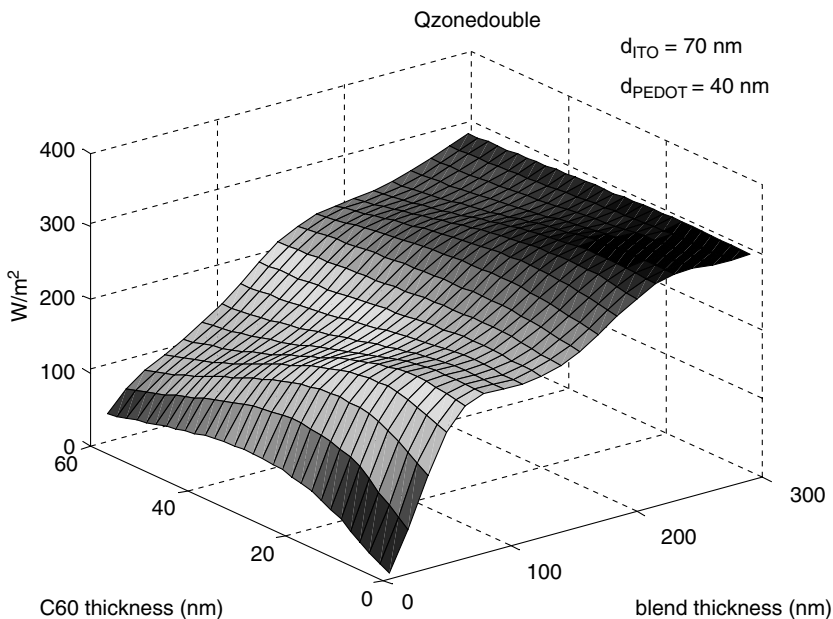
Figure 5.16. **(Color figure follows page 358)** Absorbed power per unit area, i.e., $\int Q(z)dz$ as a function of $d_{\text{blend}} \in [5,290]$ nm and $d_{C_{60}} \in [0,58]$ nm for a zone comprising all of the blend layer, and extending $\min(d_{C_{60}}, 10)$ nm into the C_{60} layer. d_{ITO} and $d_{\text{PEDOT–PSS}}$ are fixed 70 and 40 nm, respectively.

$d_{\text{blend}} = 60$ nm and $d_{C_{60}} = 10$ nm. And an even less distinct maximum somewhat above 300 W/m² is found around $(d_{\text{blend}} \; d_{C_{60}}) = (250, 10)$ nm. For more pronounced blend thicknesses, $Q_{\text{zonedouble}}$ is more or less insensitive to changes in $d_{C_{60}}$. This means that the contribution from absorption in C_{60} is negligible compared to that in the blend because of the large differences in thicknesses. But this does not mean that the **E**-field is weak in C_{60} for the same size of $d_{C_{60}}$ and d_{blend}.

In principle, it is immaterial if the diffusion zone also comprises C_{60}. The curve for this case is very similar to the curve for large d_{blend}, as seen in Figure 5.16.

For high d_{blend} and $d_{C_{60}}$ values, $Q_{\text{zonedouble}}$ seems to saturate. This is confirmed by extending (not shown) the d_{blend} interval studied. $Q_{\text{zonedouble}}$ is around 370 W/m² for $d_{\text{blend}} = 1000$ nm.

A variation in the ITO thickness has a low impact on $Q_{\text{zonedouble}}$. Surfaces are almost overlapping for $d_{\text{ITO}} = 70, 110,$ and 150 nm. Also for variation in PEDOT–PSS thickness, the impact on $Q_{\text{zonedouble}}$ is relatively low. Again surfaces as shown in Figure 5.16 for $d_{\text{PEDOT–PSS}} \in \{40,60,80,100,120\}$ nm have very similar forms. Yet, compared to the ITO case, there are larger gaps in between the surfaces. The conclusion is that $Q_{\text{zonedouble}}$ is more sensitive to the PEDOT–PSS layer, which is closer to the blend.

Thus, some conclusions can be drawn about the optimal geometry for structure c. As the dependence of $Q_{\text{zonedouble}}$ on ITO thickness is low, it is possible to take $d_{\text{ITO}} = 100$ nm because this is in accordance with the value that manufacturers state as the nominal value for the glass–ITO substrates. The PEDOT–PSS layer should be thin; therefore $d_{\text{PEDOT–PSS}} = 40$ nm is chosen. The blend layer should be as thick as possible as far as the optical optimization states. $d_{\text{blend}} = 210$ nm is a balance between this and the finite charge mobility. As the C_{60} layer is unimportant, $d_{C_{60}} = 1$ nm is used for blend layer of this thickness.

5.5.6. Sensitivity Analysis

One of the important evaluation tools of a model is an analysis studying the sensitivity to variations in parameters.[43] This is important for understanding the numerics but could also generate useful results. For structure b, Figure 5.17 shows the curvature in Q_{zone} and also the sensitivity for variation in thickness of the C_{60}-layer. This is valuable information for the device maker. For the structure as in the legend, the maximum value is given by a C_{60} thickness of around 30 nm. A 10 nm deviation from this C_{60} thickness renders 9% change in the ordinate.

5.5.7. Quantum Efficiency

Our model also allows us to reach estimates of quantum efficiencies. It follows from Equation (28) that η_A is an upper limit for the external quantum efficiency, η_{EQE}, which could be experimentally determined. The efficiency of the active layer to absorb the irradiated photons is η_{Aa}. η_{aap} is an upper limit for the internal quantum efficiency. All measures are shown in Figure 5.18 for a particular choice of thickness that most closely resembles the form of the experimental curve for structure c. $\eta_A \geq \eta_{Aa}$. For the optimal thickness combination with $d_{blend} = 210$ nm, η_A is much higher, above 90% for many wavelengths whereas EQE values can be around 50%. Obviously there is a potential for enhancing device performance if more of the absorbed photons can be utilized.

5.5.7.1. Optical Power Efficiency

As we are working with quantities measured in real units, we can also calculate how much of the total incoming light in the interval 300 to 800 nm is absorbed, a distant
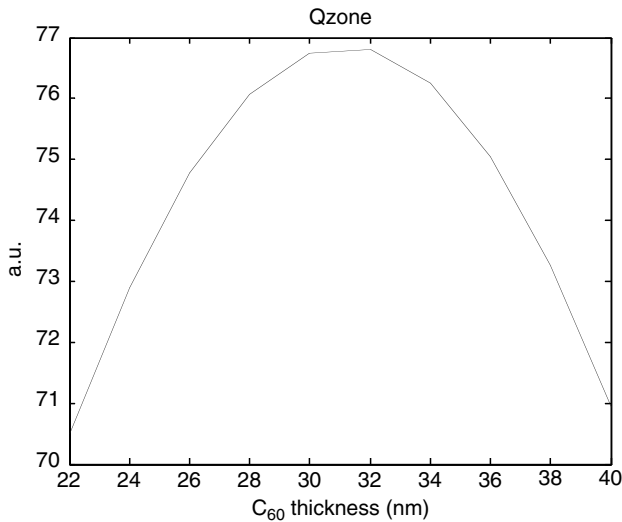

Figure 5.17. The sensitivity in Q_{zone} for variation in C_{60}-thickness for structure 2. The layer thicknesses are air/glass/ITO(90 nm)/PEDOT–PSS(90 nm)/polymer(10 nm)/C_{60}/Al. (From N.-K. Persson, M. Schubert, and O. Inganäs. *Solar Energy Materials and Solar Cells*, **83**(2–3): 169–186 (2004). With permission.)
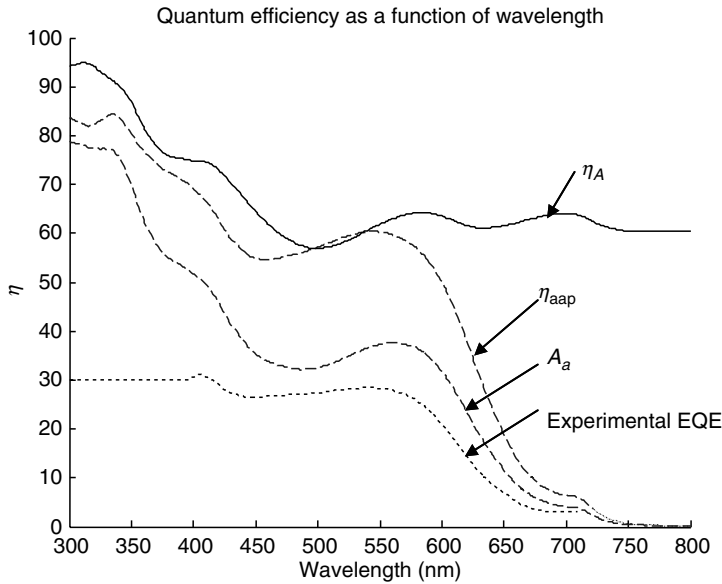
Figure 5.18. η_A (unbroken line), η_{Aa} (dashed line), η_{aap} (dashed-dotted line), and η_{EQE} (dotted) as functions of wavelength. η_A is an upper limit for η_{EQE}. η_{EQE} is experimentally determined.[35] It was not measured below 400 nm. We were aiming at $(d_{\text{ITO}}, d_{\text{PEDOT–PSS}}, d_{\text{blend}}, d_{\text{C}_{60}}) = (100, 90, 160, 1)$ nm for the experimental device. However, we find that simulations best agree in shape for the set (100, 90, 100, 1) nm, which are the shown simulation curves.

upper limit of the power conversion coefficient. The sum of the absorbed energy in the blend layer for $\lambda = [300, 800]$ nm is 303 W/m^2. Comparing with Equation (24), one gets $\eta_P = 0.48$.

5.5.8. Energy Redistribution

From a purely energetic perspective, the solar cell is a device capable of redistributing energy spatially and directionally. Radiation energy goes to radiation energy by reflection, with a change of energy flow. It is also converted to heat and other non-useful forms and finally, however beyond the present treatment, to electrical energy via the process of transport of charge. A mapping of all this is found in Figure 5.19 for structure 3. All the way up to where the polymer absorption ends, around 620 nm, most of the incoming energy is absorbed in the blend layer. Absorption in the fullerene component in the blend extends the tail to 720 nm. Reflection is moderate in this region, except for a peak at 450 nm, where it reaches 30%, coinciding with a dip in the absorption of the blend. The general view is that the polymer and its $k(\lambda)$ dependence manifest itself in the energy redistribution behavior of the whole component. $k(\lambda)$ for the blend layer was seen in Figure 5.9. Reflection losses are growing when the absorption of the blend is ceasing. Disadvantageous absorption in ITO and PEDOT–PSS is low for lower wavelengths, but increases in the band gap (longer wavelengths) of the blend. Noteworthy is the great part of absorption taken by the ITO above 650 nm. It can be explained to be due to Beer–Lambert absorption in the material that is foremost to the irradiation, but might also be due to an
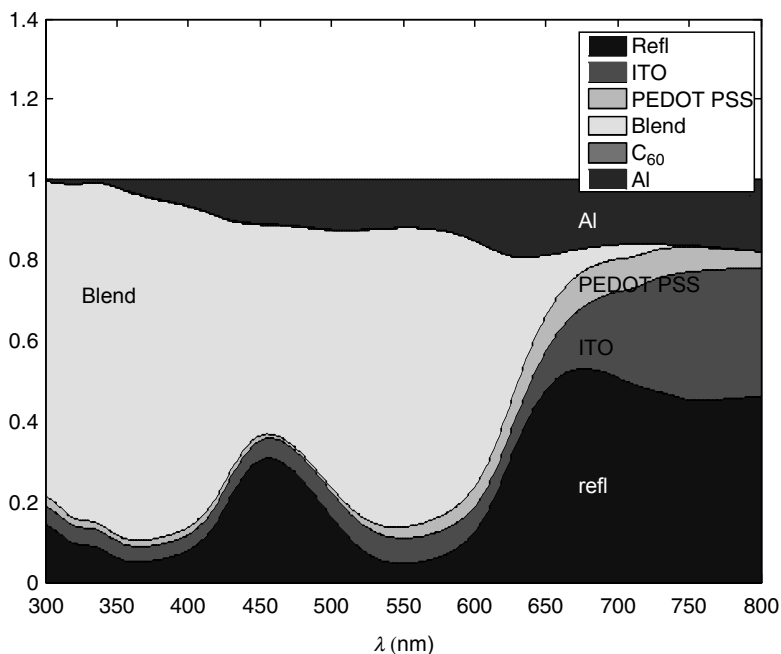
Figure 5.19. (Color figure follows page 358) Redistribution of the incoming irradiation on reflection and layerwise absorption for structure 3. The structure is (d_{ITO}, $d_{PEDOT–PSS}$, d_{blend}, $d_{C_{60}}$) = (100, 40, 210, 1) nm. As the C_{60} is very thin, it is not seen in the diagram. The curve is free from differences due to different number of irradiated photons.

overestimated α_{ITO}. Aluminium is increasing its share with increasing wavelength. It is as high as 18% for 620 nm.

5.6. SUMMARY

Optical modeling is important in two aspects — it gives insight into properties that are out of reach for direct measurements such as the $|E|^2$ profile, and provides guidance for the device manufacturer. Besides, in a couple of hours on an ordinary Macintosh or PC, the computer runs through thousands of different device geometries. This is far beyond what can be performed experimentally.

By computer-based simulation, it has been possible to examine the optical processes of the PPVD. The modeling has been based on a number of assumptions such as homogeneous layers, sharp and planar interfaces, scattering free optics, coherence in the stack part of the device, and incoherence when adding energies across the substrate. The model, which has layer thickness, layer dielectrical functions, and exciton diffusion length as input, allows us to optimize the performance by examining a large number of geometries, i.e., a set of thicknesses. The criterion has been to reach as high energy absorption in the exciton diffusion zone layer as possible.

In this chapter, we have reported on modeling of two kinds of photovoltaic devices having a layered geometry, both with a polyfluorene–copolymer as the active material and C_{60} as the acceptor. Structure b consisted of a pure polymer layer and a

pure C_{60} layer. Structure c had a blended polymer–C_{60} derivative layer in the weight ratio 1:4 with an added pure C_{60} layer.

It is assumed that due to the proximity of polymer and fullerene, the whole of the blend layer, and 10 nm in the C_{60} contribute to the photocurrent. It is also assumed that every point in the blend and in the relevant part of C_{60} contribute equally well, according to the square modulus field distribution and α and n. For structure b, a diffusion zone is defined, expanding 10 nm into the polymer and 10 nm into the C_{60} counted from the interface between these materials.

Thin film theory in a matrix formalism enables the extraction of the impact of reflection and interference on the optical electric field. $|E|^2$ as a function of depth into the device is presented. The model lets us predict, for example, an optimal C_{60}-thickness when light is assumed to be both polychromatic and distributed following solar irradiation. The value reached is 50 nm for structure 2 and 0 nm for structure 3. It is also possible to see the sensitivity for the variation from this value. The curves, such as that in Figure 5.17, are relatively flat making the diode tolerant towards mistakes in the process step of adding the C_{60} layer. In the same manner, the other layers can be analyzed.

For structure c, having only optical constraints, i.e., maximizing absorption in the active layer, the result is that the thicker the blend layer the more the absorption. This is not enough for finding an upper limit of d_{blend}. Therefore, electrical modeling is also necessary for the overall maximum performance.

A good illustration of the potential of simulation is the energy redistribution diagram that summarizes all the layers' share of absorbed energy. For wavelengths up to where the polymer ends absorbing, the major part is indeed taken by the blend layer. The total structure related reflectance is calculated. For some wavelength intervals it is very low, 5% for $\lambda = 550$ nm. It is in many parts of the spectrum below 10%, but reaches above 50% in the high-wavelength range where the copolymer has ceased to absorb.

REFERENCES

1. K. Hartt. Mathematical modeling. In *Encyclopedia of Applied Physics*. VCH Publishers, 1994, pp. 417–420.
2. B. E. Gillett. *Introduction to Operations Research*. McGraw-Hill, 1976.
3. D. T. Philips, A. Ravindran, and J. J. Solberg. *Operations Research: Principles and Practice*. John Wiley & Sons, 1976.
4. C. Heine and R. Morf. Submicrometer gratings for solar energy applications. *Applied Optics* **34**(14):2476–2482 (1995).
5. L. S. Roman, O. Inganäs, T. Granlund , et al. Trapping light in polymer photodiodes with soft embossed gratings. *Advanced Materials* **12**(3):189–195 (2000).
6. J. Nelson. Organic photovoltaic films. *Current Opinion in Solid State & Materials Science* **6**(1):87–95 (2002).
7. P. Peumans, A. Yakimov, and S. R. Forrest. Small molecular weight organic thin-film photodetectors and solar cells. *Journal of Applied Physics* **93**(7):3693–3723 (2003).
8. A. K. Ghosh, D. L. Morel, T. Feng, R. F. Shaw, and C. A. Rowe Jr. Photovoltaic and rectification properties of Al/Mg phthalocyanine/Ag Schottky-barrier cells. *Journal of Applied Physics* **45**(1):230–236 (1974).
9. M. G. Harrison, J. Grüner, and G. C. W. Spencer. Analysis of the photocurrent action spectra of MEH-PPV polymer photodiodes. *Physical Review B (Condensed Matter)* **55**(12):7831–7849 (1997).

10. A. K. Ghosh and T. Feng. Cyanine organic solar cells. *Journal of Applied Physics* **49**(12):5982–5989 (1978).

11. L. A. A. Pettersson, L. S. Roman, and O. Inganäs. Quantum efficiency of exciton-to-charge generation in organic photovoltaic devices. *Journal of Applied Physics* **89**(10):5564–5569 (2001).

12. N.-K. Persson, M. Schubert, and O. Inganäs. Optical modeling of a layered photovoltaic device with a polyfluorene derivative/fullerene as the active layer. *Solar Energy Materials and Solar Cells* **83**(2–3):169–186 (2004).

13. H. Hoppe, N. Arnold, N. S. Sariciftci, and D. Meissner. Modeling the optical absorption within conjugated polymer/fullerene-based bulk-heterojunction organic solar cells. *Solar Energy Materials and Solar Cells* **80**(1):105–113 (2003).

14. J. Rostalski and D. Meissner. Photocurrent spectroscopy for the investigation of charge carrier generation and transport mechanisms in organic p/n junction solar cells. *Solar Energy Materials and Solar Cells* **63**:37–47 (2000).

15. H. A. MacLeod. *Thin Film Optical Filters*. Institute of Physics Publishing, 2001.

16. L. Vriens and W. Rippens. Optical constants of absorbing thin solid films on a substrate. *Applied Optics* **22**(24):4105–4110 (1983).

17. B. Harbecke. Coherent and incoherent reflection and transmission of multilayer structures. *Applied Physics B* **39**(3):165–170 (1986).

18. E. Elizalde and F. Rueda. On the determination of the optical constants $n(\lambda)$ and $\alpha(\lambda)$ of thin supported films. *Thin Solid Films* **122**(1):45–57 (1984).

19. R. F. Potter. Basic parameters for measuring optical properties. In E. D. Palik (ed.), *Handbook of Optical Constants of Solids I*. Academic Press, 1985, pp. 11–34.

20. E. D. Palik. Errata. In E. D. Palik (ed.), *Handbook of Optical Constants of Solids II*. Academic Press, 1991, pp. 8–11.

21. A. H. M. Holtslag and P. M. L. O. Scholte. Optical measurement of the refractive index, layer thickness, and volume changes of thin films. *Applied Optics* **28**(23):5095–5104 (1989).

22. J. J. M. Halls, K. Pichler, R. H. Friend, S. C. Moratti, and A. B. Holmes. Exciton diffusion and dissociation in a poly(*p*-phenylenevinylene)/C_{60} heterojunction photovoltaic cell. *Applied Physics Letters* **68**(22):3120–3122 (1996).

23. J. J. M. Halls. Photoconductive Properties of Conjugated Polymers. PhD dissertation, St John's College, Cambridge, UK, 1997.

24. L. A. A. Pettersson, L. S. Roman, and O. Inganäs. Modeling photocurrent action spectra of photovoltaic devices based on organic thin films. *Journal of Applied Physics* **86**(1):487–496 (1999).

25. T. Stubinger and W. Brutting. Exciton diffusion and optical interference in organic donor–acceptor photovoltaic cells. *Journal of Applied Physics* **90**(7):3632–3641 (2001).

26. J. D. Jackson. Electrodynamics, Classical. In *Encyclopedia of Applied Physics*. VCH Publishers.1994, pp. 283–285.

27. W. Greiner. *Classical Electrodynamics*. Springer, 1996.

28. L. D. Landau, E. M.Lifshitz, and L. P. Pitaevskii. *Electrodynamics of Continous Media*. Pergamon Press, 1984.

29. Key Center of Photovoltaic Engineering UNSW, Australia. UNSW Air Mass 1.5 Global Spectrum. www.pv.unsw.edu.au/am1.5.html

30. A. C. Arias, J. D. MacKenzie, R. Stevenson, J. J. M. Halls, M. Inbasekaran, E. P. Woo, D. Richards, and R. H. Friend. Photovoltaic performance and morphology of polyfluorene blends: a combined microscopic and photovoltaic investigation. *Macromolecules* **34**(17):6005–6013 (2001).

31. M. Svensson, F. Zhang, S. Veenstra, W. Verhes, J. C. Hummelen, J. Kroon, O. Inganäs, and M. R. Andersson. High performance polymer solar cells of an alternating polyfluorene copolymer and a fullerene derivative. *Advanced Materials* **15**(12):988–991 (2003).

32. R. Pacios, D. D. C. Bradley, J. Nelson, and C. J. Brabec. Efficient polyfluorene based solar cells. *Synthetic Metals* **137**(1–3):1469–1470 (2003).

33. M. Leclerc. Polyfluorenes: twenty years of progress. *Journal of Polymer Science: Part A: Polymer Science* **39**(17):2867–2873 (2001).

34. A. Meisel, T. Miteva, H. G. Nothofer, W. Knoll, D. Sainova, D. Neher, G. Nelles, A. Yasuda, F. C. Grozema, T. J. Savenije, B. R. Wegewijs, L. D. A. Siebbeles, J. M. Warman, and U. Scherf. 2001. Anisotropy of the optical and electrical properties of highly-oriented polyfluorenes. In *Polytronic 2001, Proceedings*. IEEE New York, pp. 284–290.

35. O. Inganäs, F. Zhang, X. Wang, A. Gadisa, N.-K. Persson, M. Svensson, E. Perzon, W. Mammo, and M. R. Andersson. Alternating fluorene copolymer-fullerene blend solar cells. In S.-S. Sun and N. S. Sariciftci (eds), *Organic Photovoltaics: Mechanisms, Materials and Devices*, CRC Press, Boca Raton, FL, USA, 2005, pp. 389–404.

36. N.-K. Persson, H. Arwin, and O. Inganäs. Optical optimization polyfluorene–fullerene blend photodiodes. Submitted for publication.

37. A. Haugeneder, M. Neges, C. Kallinger, W. Spirkl, U. Lemmer, J. Feldmann, U. Scherf, E. Harth, A. Gugel, and K. Mullen. Exciton diffusion and dissociation in conjugated polymer fullerene blends and heterostructures. *Physical Review B* (*Condensed Matter*) **59**(23):15346–15351 (1999).

38. M. Theander, A. Yartsev, D. Zigmantas, V. Sundström, W. Mammo, M. R. Andersson, and O. Inganäs. Photoluminescence quenching at a polythiophene/C60 heterojunction. *Physical Review B* (*Condensed Matter*) **61**(19):12957–12963 (2000).

39. L. A. A. Pettersson, F. Carlsson, O. Inganäs, and H. Arwin. Spectroscopic ellipsometry studies of the optical properties of doped poly(3,4-ethylenedioxythiophene); an isotropic metal. *Thin Solid Films* **313–314**:356–361 (1998).

40. D. Y. Smith. The optical properties of metallic aluminium. In *Handbook of Optical Constants of Solids*. Academic Press, 1998.

41. J. Bartella, J. Schroeder, and K. Witting. Characterization of ITO- and TiO_xN_y films by spectroscopic ellipsometry, spectraphotometry and XPS. *Applied Surface Science* **179**(1–4):182–191 (2001).

42. L. Roman, W. Mammo, L. A. A. Pettersson, M. R. Andersson, and O. Inganäs. High quantum efficiency polythiophene/C_{60} photodiodes. *Advanced Materials* **10**(10):774–777 (1998).

43. R. Beare. *Mathematics in Action: Modeling in the Real World Using Mathematics*. Chartwell-Bratt, 1997.